Research Article
doi.org/10.1002/celc.202500286



www.chemelectrochem.org

# Beyond Conventional Coatings: Melt-Infiltration of Antiperovskites for High-Voltage All-Solid-State Batteries

Philip Henkel, Ruizhuo Zhang, Rajib Sahu, Christian Kübel, Jürgen Janek, Aleksandr Kondrakov,* and Torsten Brezesinski*

Solid-state batteries (SSBs) have emerged as promising candidates for next-generation energy-storage solutions, particularly for electric vehicle applications. To overcome challenges related to interfacial stability and electro-chemo-mechanical degradation during operation, the development of protective surface coatings for cathode active materials (CAMs) is essential. Lithium-rich antiperovskites (LiRAPs) exhibit a unique set of beneficial properties, notably a high ionic partial conductivity at room temperature, enabling the deployment of advanced coating techniques via cost-effective and environmentally benign methods. In the present work, the application of LiRAP coatings to a layered Ni-rich CAM, namely $LiNi_{0.85}Co_{0.1}Mn_{0.05}O_2$ (NCM85), is examined, utilizing a low-temperature and solvent-free approach. The effectiveness of the procedure is evaluated through microscopy analyses and electrochemical performance assessments. The results demonstrate a significant improvement in cyclability, highlighting the potential of LiRAP-based surface coatings for enhancing the performance and longevity of high-capacity cathodes in SSB systems.

## 1. Introduction

Interest in solid-state batteries (SSBs) has grown significantly in the past, as they represent one of the most promising alternatives for electrochemical energy storage, particularly for electric vehicle applications.[1,2] Compared to conventional lithium-ion batteries (LIBs), SSBs offer distinct advantages, including higher energy density, improved safety, and environmental benefits arising mostly from the use of solid electrolytes (SEs). Additionally, they enable optimized pack designs and eliminate the need for advanced cooling systems, thereby contributing to their economic attractiveness.[3–7] Nevertheless, SSBs continue to face considerable challenges inherent to solid systems, notably the (electro)chemical degradation at the cathode active material (CAM)|SE interface, leading to capacity fading.[8,9] Volume changes in CAMs during cycling further exacerbate these issues by causing particle fracture and contact loss, while outgassing at high states of charge contributes to the cathode–electrolyte interphase (CEI) formation.[2,10,11] Moreover, commonly employed thiophosphate SEs, such as $Li_6PS_5Cl$ (LPSCl), $Li_{10}GeP_2S_{12}$ (LGPS), or $Li_3PS_4$ (LPS), exhibit limited electrochemical stability windows, leading to electrochemical oxidation and adverse side reactions with state-of-the-art (high-capacity) CAMs, such as lithium nickel manganese cobalt oxides (NCMs or NMCs), lithium nickel cobalt aluminum oxides (NCAs), or $LiNiO_2$ (LNO). These reactions increase interfacial resistance and hinder lithium diffusion, ultimately impeding effective charge transfer across the CAM|SE interface.[9,12–14]

To address these challenges, protective coatings on CAMs have been extensively explored. Methods such as dry coating (e.g., milling techniques), wet coating (e.g., sol–gel, solvothermal, hydrothermal techniques), and physical deposition processes (e.g., atomic layer deposition [ALD], pulsed layer deposition [PLD], chemical vapor deposition [CVD]) aim to achieve uniform surface coverage and modifications to complex substrate geometries.[15–17] Oxides, including $Li_3PO_4$, $Li_2ZrO_3$, and particularly $LiNbO_3$, known for their reasonably high ionic conductivity, low electronic partial conductivity, and high overall stability, have shown promising potential as coating materials.[18–21] Aside from that, lithium-rich antiperovskites (LiRAPs), such as $Li_3OCl$, $Li_2OHCl$,

P. Henkel, R. Zhang, R. Sahu, J. Janek, A. Kondrakov, T. Brezesinski
Battery and Electrochemistry Laboratory (BELLA)
Institute of Nanotechnology
Karlsruhe Institute of Technology (KIT)
Kaiserstr. 12, 76131 Karlsruhe, Germany
E-mail: aleksandr.kondrakov@basf.com
torsten.brezesinski@kit.edu

R. Sahu, C. Kübel
Karlsruhe Nano Micro Facility (KNMFi)
Institute of Nanotechnology
Karlsruhe Institute of Technology (KIT)
Kaiserstr. 12, 76131 Karlsruhe, Germany

C. Kübel
Institute of Materials Science
Technical University Darmstadt (TUDa)
Peter-Grünberg-Str. 2, 64287 Darmstadt, Germany

J. Janek
Institute of Physical Chemistry & Center for Materials Research (ZfM/LaMa)
Justus-Liebig-University Giessen
Heinrich-Buff-Ring 17, 35392 Giessen, Germany

A. Kondrakov
BASF SE
Carl-Bosch-Str. 38, 67056 Ludwigshafen, Germany

Supporting information for this article is available on the WWW under https://doi.org/10.1002/celc.202500286

and $Li_2OHBr$, to name some, have gained attention in recent years, primarily owing to their high ionic conductivity, exceeding 1 mS $cm^{-1}$ at room temperature, chemical stability with lithium metal, and adaptability.[22–24] Produced via cost-effective, environmentally friendly synthesis routes, LiRAPs are attractive for large-scale manufacturing.[25–27] To date, they have predominantly been utilized as SEs rather than CAM coatings, despite their favorable properties. However, the hygroscopic nature of these materials, especially of H-free $Li_3OCl$, limits their application and requires strict avoidance of moisture and inert processing conditions.[24,28,29]

Herein, we report on the melt-infiltration method utilizing LiRAPs, specifically $Li_2OHCl_{0.5}Br_{0.5}$ and $Li_2OHCl$, as dry coatings on $LiNi_{0.85}Co_{0.1}Mn_{0.05}O_2$ (NCM85) cathodes. Their relatively low melting point of about 300 °C makes them attractive for the application of melt-infiltration to commonly used CAMs, such as Ni-rich NCMs, since these materials can be considered inert at moderate temperatures.[26,30,31] Unlike conventional dry-coating methods, which typically suffer from nonuniform distribution (surface coverage/thickness), melt-infiltration ensures that the coating material under study is in a liquid state, capable of uniformly covering the CAM particles and effectively infiltrating surface pores. The latter aims at preventing void and crack formation within the CAM, thus stabilizing the material during battery operation.

## 2. Results and Discussion

The antiperovskites $Li_2OHCl$ and $Li_2OHCl_{0.5}Br_{0.5}$ were synthesized following established procedures reported by Hood et al., involving facile solid-state reactions using stoichiometric mixtures of LiOH and LiCl or LiCl and LiBr.[32] Upon heating to 350 °C, a eutectic reaction takes place. Rapid cooling as the final step is crucial for the preparation of LiRAPs, strongly affecting defect density and, therefore, ionic conductivity.[22,32,33] The impact of various cooling rates on properties and the effectiveness of these materials as protective coatings was elucidated in subsequent electrochemical tests.

X-ray diffraction (XRD) patterns and corresponding Rietveld plots for $Li_2OHCl$ and $Li_2OHCl_{0.5}Br_{0.5}$ are presented in **Figure 1**a,b, respectively, indicating that both crystallize in a cubic (perovskite) structure within the space group $Pm-3m$ and exhibit similar structural characteristics.[34] $Li_2OHCl$ and $Li_2OHCl_{0.5}Br_{0.5}$ have been shown to possess a disordered antiperovskite framework, in which the hydroxyl group occupies the octahedral center. The $Li^+$ ions reside on partially occupied sublattices, enabling high mobility due to low migration barriers and defect-rich environments, especially in quenched samples.[33] Of note, compounds within the $Li_2OHCl_xBr_{1-x}$ series have been synthesized by adjusting precursor stoichiometries accordingly.[30] In general, the lattice parameter $a$ offers an indication of chlorine substitution by bromine, as literature reports parameters of $a = 3.910$ Å for $Li_2OHCl$ and $a = 4.047$ Å for $Li_2OHBr$,[30,35] in good agreement with those determined in the present work (see Table S1, Supporting Information). The lattice parameter of $Li_2OHCl_{0.5}Br_{0.5}$ [$a = 3.9774(1)$ Å] was found to lie between the aforementioned values, supporting the 50% substitution of chlorine by bromine ($x = 0.5$ in $Li_2OHCl_xBr_{1-x}$). Rietveld analysis further revealed the presence of minor impurity reflections at 15.7°, 22.3°, and 26.5° $2\theta$ in the case of $Li_2OHCl$. These can be attributed to residual LiCl, accounting for about 0.8 wt%. In contrast, the diffraction data collected from $Li_2OHCl_{0.5}Br_{0.5}$ indicate high purity without detectable precursor remnants or secondary phases.

Scanning electron microscopy (SEM) was employed to examine the coating distribution on the NCM85 secondary particles. The CAMs analyzed primarily include $Li_2OHCl_{0.5}Br_{0.5}$@NCM85, hereafter referred to as LHCB@NCM85, with coating contents of 0.75 and 1.0 wt%, both before and after the melt-infiltration process at 350 °C. We note that “before melt-infiltration” can be considered as “after dry mixing” of NCM85 and LHCB by ball milling. The SEM images recorded before melt-infiltration revealed agglomeration of the coating material on the NCM85 top surface, as indicated by the regions highlighted in Figure 1c,e. In principle, the agglomerated particles should be in a liquid state at 350 °C and fully cover the accessible NCM85 surface prior to cooling. The addition of 1 wt% LHCB was calculated to result in a coating of thickness about 14 nm (assuming dense NCM85 secondary particles). Indeed, after melt-infiltration, the agglomerates disappeared, and the presence of a kind of shell on the secondary particles was observed, likely corresponding to the LHCB coating, as illustrated in Figure 1d,f. These findings suggest that the melt-infiltration process, combined with rapid cooling, indeed enables the formation of a relatively uniform and dense coating.

Energy-dispersive X-ray (EDX) spectroscopy further provided elemental mapping before and after melt-infiltration (see Figure S1, Supporting Information). Prior to melt-infiltration, the EDX data exhibited strongly localized signals of chlorine and bromine, corresponding to agglomerated coating material and overshadowing the presence of dispersed LHCB particles. After melt-infiltration, the elemental distribution appeared much more even, emphasizing the effectiveness of the heating step in improving coating coverage and uniformity.

Scanning transmission electron microscopy (STEM) analysis was performed to qualitatively assess structure and thickness of the LHCB layer on the NCM85 particles (with 1.0 wt% coating content), again both before and after melt-infiltration. Bright-field TEM images taken prior to melt-infiltration revealed both agglomerates of LHCB particles adhering as discrete clusters to the CAM and uncoated regions exposing the pristine NCM85 surface, as illustrated in **Figure 2**a,b. After melt-infiltration, a consistent coating of thickness 8–10 nm was observed on the NCM85 surface, as shown in Figure 2c–e. This value is slightly lower than predicted by theoretical calculations, likely due to some inhomogeneities in coating thickness. Additionally, the previously mentioned residual LiCl may indicate that the reaction did not proceed to completion, potentially resulting in a reduced amount of deposited material. The coating itself exhibited distinct interplanar spacings of 2.5 Å (310 plane), consistent with the refined XRD data, whereas the underlying substrate displayed spacings of 4.8 Å (003 plane), see Figure 2f. As evident, the respective fast

Research Article
doi.org/10.1002/celc.202500286



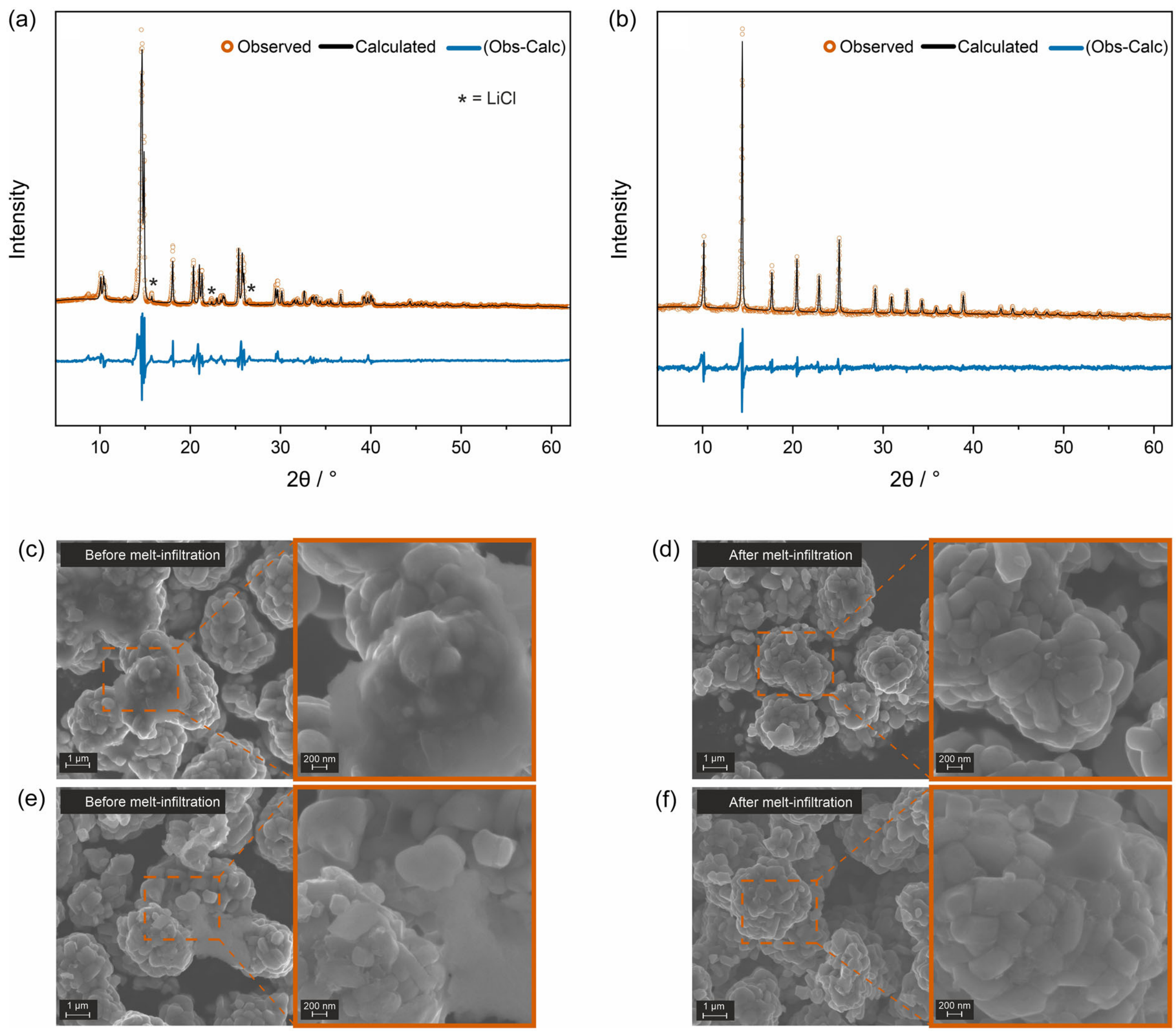


**Figure 1.** a) Rietveld refinement of XRD data collected from $Li_2OHCl$. The asterisks at 15.7°, 22.3°, and 26.5° $2\theta$ denote the presence of about 0.8 wt% of unreacted LiCl. b) Rietveld refinement of XRD data collected from $Li_2OHCl_{0.5}Br_{0.5}$. SEM images at different magnifications of LHCB@NCM85 with 0.75 wt% coating content c) before and d) after melt-infiltration. SEM images at different magnifications of LHCB@NCM85 with 1.0 wt% coating content e) before and f) after melt-infiltration.

Fourier transformation (FFT) patterns in the insets of Figure 2e exhibit distinct reflection spots, confirming the crystalline nature of both LHCB and NCM85. High-angle annular dark field (HAADF) imaging further corroborated the enhanced coating distribution after melt-infiltration, based on the mapping results in Figure 2g–n. Integrated STEM EDX spectra revealing characteristic element-specific peaks are available in the Supporting Information. As expected, distribution analysis revealed significant heterogeneity prior to melt-infiltration, with values fluctuating from virtually zero to about 2 wt% for chlorine and bromine (see Figure S2, Supporting Information). However, the elemental distribution improved considerably upon melt-infiltration, primarily ranging between 0.4 and 0.7 wt%, with localized concentrations of bromine reaching up to 2.4 wt% and chlorine up to 1.0 wt% at the grain boundaries, as illustrated in Figure 2h. Overall, the data still suggests higher (localized) concentrations of bromine than chlorine, despite the nominal equimolar ratio. This discrepancy may originate from preferential segregation. Zheng et al. found that the grain-boundary conductivity of melt-cast $Li_2OHCl$ is slightly higher than that of $Li_2OHBr$, indicating that composition affects interfacial charge transport. This, in turn, may suggest that accumulation of $Br^-$ at the grain boundaries during recrystallization somewhat hinders lithium transport while simultaneously leading to an apparent enrichment in STEM EDX analysis.[36] Nevertheless, these observations highlight the effectiveness of the melt-infiltration method in realizing a relatively uniform and consistent coating distribution.

Electrochemical measurements were conducted on pellet-stack SSB cells utilizing argyrodite $Li_6PS_5Cl$ as the SE at an operating temperature of 45 °C and at an external pressure of 81 MPa within the voltage window of 2.3–3.7 V versus In/InLi (equivalent to about 2.9–4.3 V vs $Li^+$/Li). As mentioned above, the cooling step strongly affects the ionic conductivity of antiperovskite materials. Rapid cooling typically results in "high" ionic conductivity, whereas slow

Research Article
doi.org/10.1002/celc.202500286


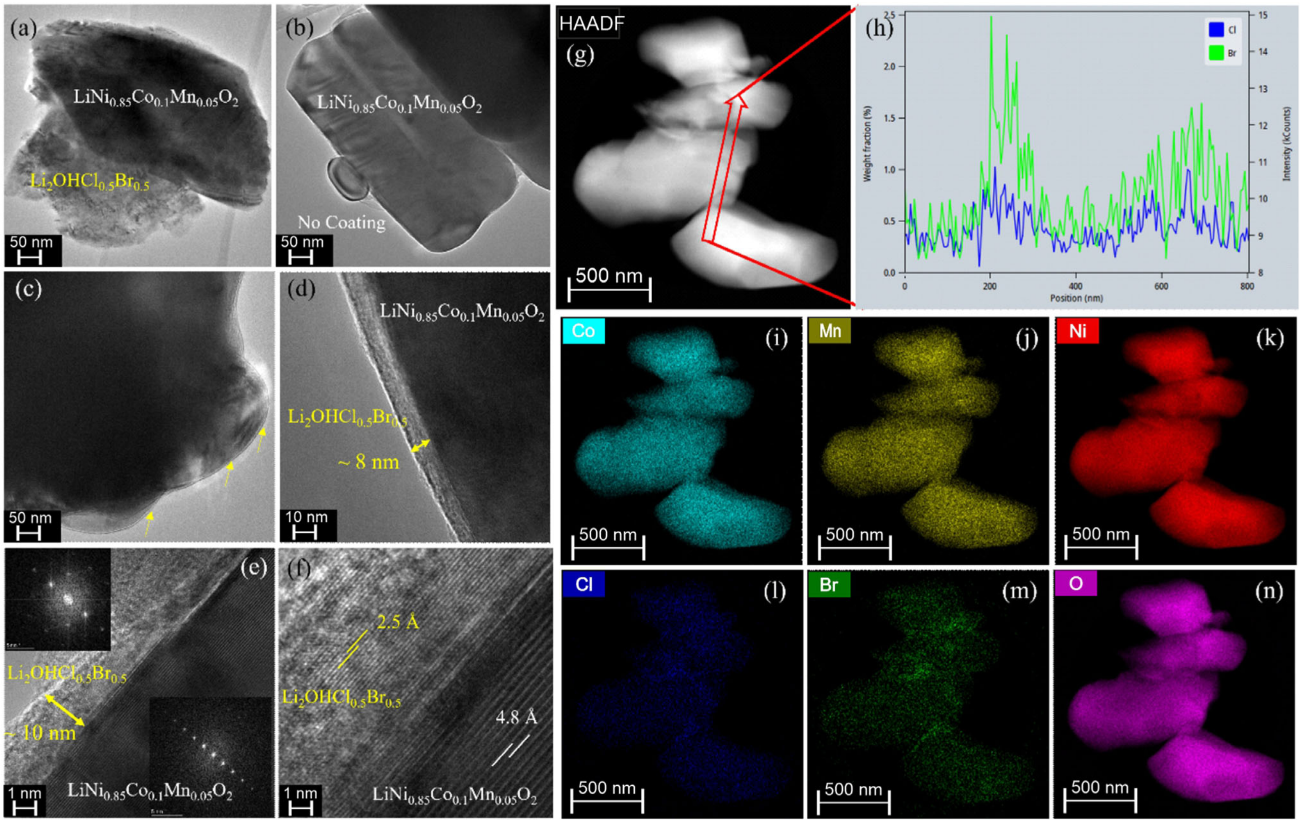


**Figure 2.** Bright-field TEM images of LHCB@NCM85 with 1.0 wt% coating content a,b) before and c–f) after melt-infiltration with corresponding FFT patterns. g) HAADF STEM image of a coated particle after melt-infiltration. h) Weight-fraction distribution of bromine and chlorine across the particle, as indicated in (g). i–n) Elemental maps corresponding to (g).

cooling promotes formation of a better-ordered structure with fewer vacancies, limiting lithium mobility.[33] Here, LHCB@NCM85 with 1.0 wt% coating content was evaluated after undergoing two distinct cooling processes, namely 1) quenching in liquid nitrogen and 2) gradual cooling over 2 h in an oven. In fact, the rapidly cooled material was found to deliver high initial specific capacities at 0.1 C, achieving $q_{ch} \approx 233$ mAh/$g_{CAM}$ and $q_{dis} \approx 194$ mAh/$g_{CAM}$ ($\approx$2.1 mAh $cm^{-2}$), as demonstrated in **Figure 3a**. By contrast, the slowly cooled material demonstrated lower specific capacities, reaching about 220 mAh/$g_{CAM}$ and 167 mAh/$g_{CAM}$ ($\approx$1.8 mAh $cm^{-2}$) for charge and discharge, respectively. Accordingly, the Coulomb efficiency of LHCB@NCM85 (rapid) was notably higher at 83%, compared to 76% observed for LHCB@NCM85 (slow). Rate capability and long-term stability tests further underscored the superior performance of the rapidly cooled material, as illustrated in Figure 3b. After 100 cycles, LHCB@NCM85 (rapid) maintained a specific discharge capacity of $q_{dis} \approx 139$ mAh/$g_{CAM}$ at 0.2 C, while LHCB@NCM85 (slow) experienced capacity fading to $q_{dis} \approx 89$ mAh/$g_{CAM}$. To explain this marked difference in cycling performance, we assume two possibilities: 1) a higher defect density and enhanced ionic conductivity in the rapidly cooled material, and 2) slower cooling results in phase separation of LHCB and particle agglomeration, likely impeding charge transport. Hence, rapid cooling post-melting is critical to achieving a robust coating, thereby positively affecting electrochemical performance and structural stability.

The electrochemical stability window of LiRAPs has been widely debated, with literature proposing "stable" operation below 3.0 V versus $Li^+$/Li. To address this, cyclic voltammetry (CV) measurements were conducted on LHCB/Super C65 carbon composite electrodes at 45 °C and within a voltage window of 2.0–3.7 V versus In/InLi, employing $Li_6PS_5Cl$ as the SE separator (see Figure S3, Supporting Information). In the initial cycle, a pronounced anodic peak emerged around 3.5 V, indicative of irreversible side reactions. This peak diminished in subsequent cycles, with a gradual shift in onset potential toward higher values, reaching about 3.65 V by the fourth cycle. This behavior might lead to a progressive electrochemical stabilization, potentially explained by the formation of a decomposition interphase (CEI) at the NCM85|LHCB interface, likely also driven, at least in part, by oxygen evolution from the layered CAM.[32,37] It should be noted that $Li_6PS_5Cl$ also undergoes (electro)chemical degradation in the same operating voltage window, forming decomposition products, such as polysulfides and/or $SO_x$/$PO_x$ species. Consequently, side reactions occurring between SE and LHCB should also be taken into account.[38]

Subsequent electrochemical studies evaluated the effectiveness of $Li_2OHCl$ (LHC), $Li_2OHCl_{0.5}Br_{0.5}$ (LHCB), and mixed coatings of LHCB and $LiNbO_3$ (LNbO) at ratios of 0.5:0.5 wt%

Chemistry Europe
European Chemical Societies Publishing

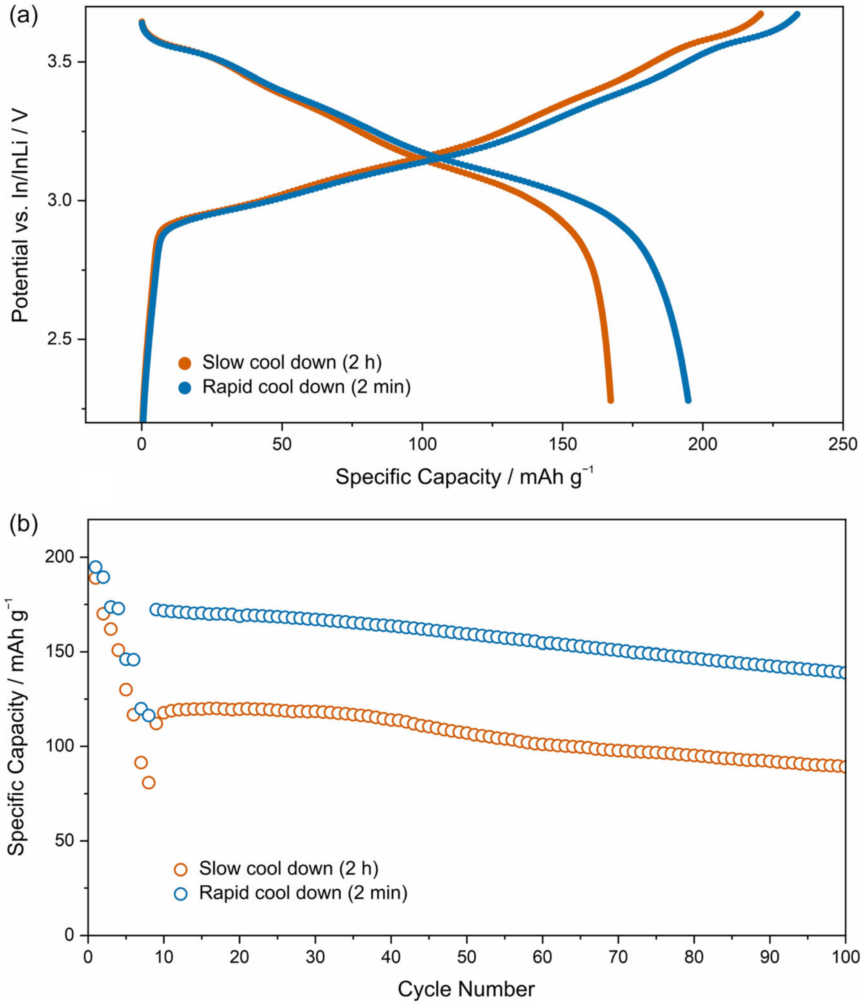


**Figure 3.** a) First-cycle charge–discharge curves of LHCB@NCM85 cathodes (1.0 wt% coating content; slowly and rapidly cooled to room temperature) in thiophosphate-based SSB cells at 45 °C and 0.1 C rate. b) Rate-performance testing at 0.1, 0.2, 0.5, and 1.0 C (two cycles each) followed by long-term cycling at 0.2 C.

[LHCB:LNbO(0.5)] and 1.0:1.0 wt% [LHCB:LNbO(1.0)] on the NCM85. The coating content in the LHC@NCM85 and LHCB@NCM85 samples was controlled at 1.0 wt% due to better overall performance (see Figure S4, Supporting Information). In general, lithium-containing oxide coatings are known for their potential to stabilize the CAM|SE interface, thereby expanding the electrochemical stability window in SSBs. However, the LHCB:LNbO@NCM85 cathodes delivered the lowest specific discharge capacities of $q_{dis} \approx 182$ mAh/g$_{CAM}$ at 0.1 C in the initial cycle, as shown in **Figure 4a**. The LHCB@NCM85 cathode achieved around 194 mAh/g$_{CAM}$, as mentioned previously, whereas LHC@NCM85 demonstrated the highest specific discharge capacity of $q_{dis} \approx 205$ mAh/g$_{CAM}$, clearly outperforming the uncoated CAM, which delivered about 191 mAh/g$_{CAM}$. Furthermore, LHC@NCM85 exhibited the highest first-cycle Coulomb efficiency of 89%, compared to 83%, 80%, 83%, and 84% for LHCB@NCM, LHCB:LNbO(0.5)@NCM85, LHCB:LNbO(1.0)@NCM85, and uncoated NCM85, respectively. The observed enhancement may be attributed to the protective coating mitigating unfavorable reactions at the CAM|SE and CAM|Super C65 interfaces, facilitating more efficient lithium (de)intercalation. The lower initial capacities of the LHCB@NCM85 and LHCB:LNbO@NCM85 cathodes are thought to be related to somewhat hindered lithium transport. Note that the coating composition determines the ionic conductivity and therefore, contributes to this behavior.

Differential capacity (d$q$/d$V$) analysis identified the characteristic phase transitions, from hexagonal to monoclinic (H1-M), monoclinic to hexagonal (M-H2), and hexagonal to hexagonal (H2-H3), as demonstrated in Figure 4b. Notably, the LHCB:LNbO@NCM85 cathodes exhibited lower peak intensities, particularly during the critical H2-H3 transition, known for causing structural instabilities in layered Ni-rich oxide CAMs. Additionally, the H1-M transition in the thicker composite coating [LHCB:LNbO(1.0)] displayed a slight shift toward higher potentials, implying that increasing coating thickness is negatively affecting lithium diffusion kinetics. Both LHCB@NCM85 and LHC@NCM85 exhibited an electrochemical behavior reminiscent of that of uncoated NCM85, especially in the H1-M and M-H2 regions. Regardless, they delivered the highest capacity during the H2-H3 transition, whereas the uncoated

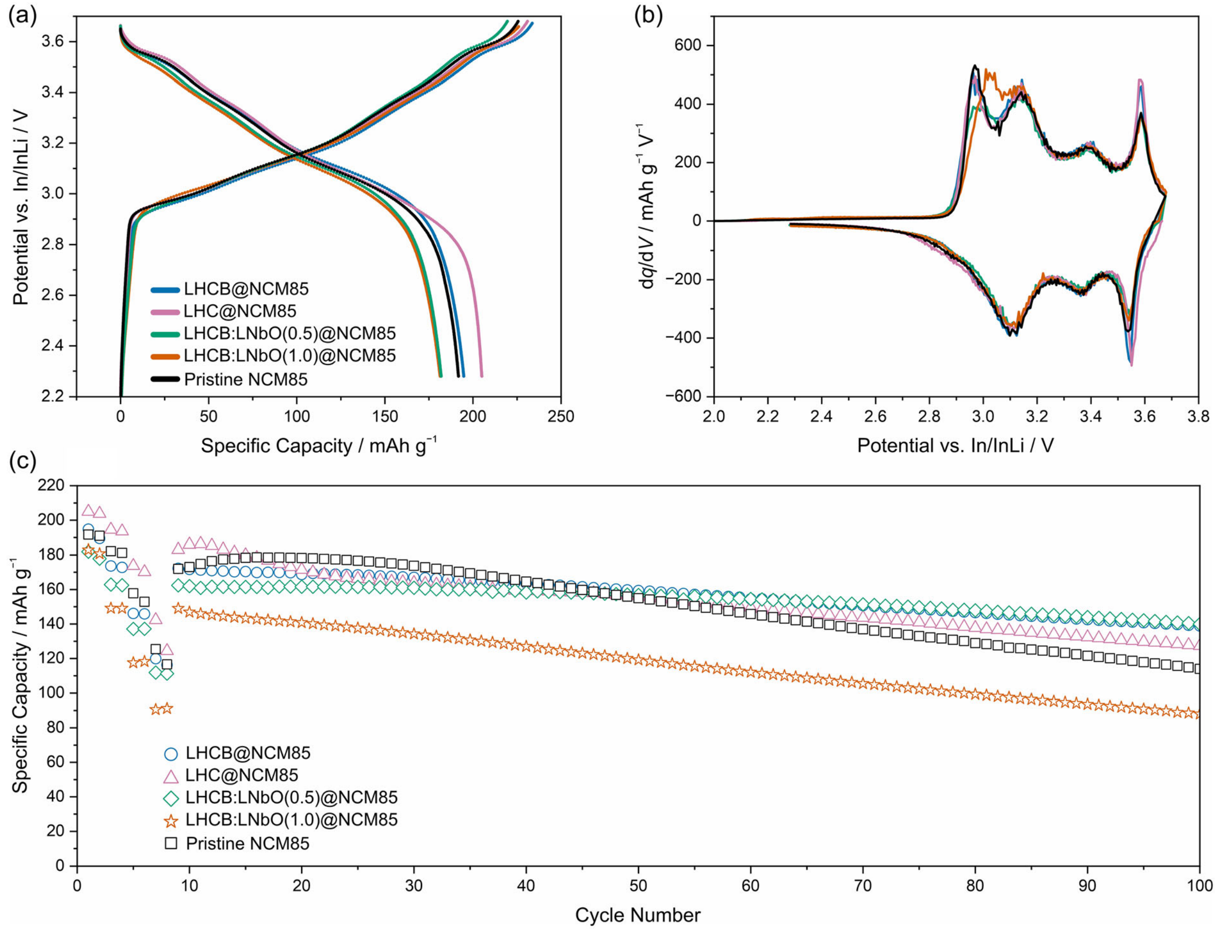


**Figure 4.** a) First-cycle charge–discharge curves of thiophosphate-based SSB cells using either LHCB@NCM85, LHC@NCM85, LHCB:LNbO(0.5)@NCM85, LHCB:LNbO(1.0)@NCM85, or uncoated NCM85 at 45 °C and 0.1 C rate. The coating content of the former two CAMs was 1.0 wt%. b) Corresponding second-cycle differential capacity curves. c) Rate-performance testing at 0.1, 0.2, 0.5, and 1.0 C (two cycles each) followed by long-term cycling at 0.2 C.

NCM85 showed a similar behavior to the LHCB:LNbO@NCM85 cathodes.

The long-term cycling performance was assessed at 0.2 C following rate capability testing at 0.1, 0.2, 0.5, and 1.0 C, as shown in Figure 4c. The uncoated NCM85 cathode was capable of delivering a specific discharge capacity of $q_{dis} \approx 114$ mAh/g$_{CAM}$ after 100 cycles, corresponding to a capacity retention of 66% (relative to the ninth cycle). The LHCB:LNbO(1.0)@NCM85 cathode exhibited the lowest specific capacity of about 88 mAh/g$_{CAM}$ (59%) among the CAMs tested in this work. LHC@NCM85, despite delivering the highest $q_{dis}$ in the initial cycle at 0.1 C, only maintained a specific discharge capacity of about 128 mAh/g$_{CAM}$ (69%). By contrast, LHCB@NCM85 achieved lower capacities than the uncoated NCM85 up to cycle 40, but delivered around 139 mAh/g$_{CAM}$ (80%) after 100 cycles. The LHCB:LNbO(0.5)@NCM85 cathode exhibited superior stability, retaining $\approx$140 mAh/g$_{CAM}$ (86%), although the initial capacities were comparatively lower. The faster fading of the LNbO-free CAMs may be related to their initially higher capacities, leading to greater chemo-mechanical stress during cycling. This likely accelerates degradation by triggering adverse side reactions. By contrast, $LiNbO_3$, as a proven coating material, may stabilize LHCB when used in combination. The higher initial capacity of LHC@NCM85 could simply be due to the higher conductivity of the antiperovskite when applied separately.

Electrochemical impedance spectroscopy (EIS) measurements conducted on cells with LHC@NCM85 or LHCB:LNbO(0.5)@NCM85 after 20 cycles at the end of charge (see Figure S5 and Table S2, Supporting Information) confirm the trends seen by indicating lower interfacial resistance of 30.9 Ω for LHC@NCM85, compared to 46.3 Ω for LHCB:LNbO(0.5)@NCM85. However, the capacity decay is more pronounced for the LNbO-free sample, presumably for the reason mentioned above, despite the initially favorable interfacial charge transfer.

These results highlight the benefits conferred by antiperovskite coatings in enhancing the cycling performance and stability of Ni-rich NCM cathodes in thiophosphate-based SSBs. Furthermore, an unusual increase in capacity was noticed over the first few cycles at 0.2 C after rate capability testing. While the underlying cause remains largely unclear, it may be related to interfacial effects. Interestingly, this behavior was most strongly observed for the uncoated NCM85, supporting the hypothesis of contact-related limitations.

Overall, the improvements are primarily attributed to structural and (electro)chemical stabilization effects provided by the protective coatings, mitigating common degradation phenomena during battery operation. However, further work is required to make antiperovskites competitive with state-of-the-art (oxide) coating materials. Nevertheless, the present study can be understood as a starting point and may serve as an inspiration for future work.

## 3. Conclusion

In this study, NCM85 secondary particles were successfully coated with LiRAPs, specifically $Li_2OHCl$ (LHC) and $Li_2OHCl_{0.5}Br_{0.5}$ (LHCB), via a melt-infiltration approach. Surface coating involved heating ball-milled blends of CAM and LiRAPs at 350 °C, i.e., above their melting point, followed by quenching to room temperature in order to suppress phase separation and promote even distribution. Characterization via XRD confirmed the cubic structure of the synthesized LiRAPs. Both SEM and TEM imaging indicated the presence of a relatively uniform coating of thickness 8–10 nm after melt-infiltration, while samples examined after dry mixing, or, in other words, prior to melt-infiltration, suffered from agglomeration of LiRAP particles, as somewhat expected. Electrochemical testing further demonstrated that rapid cooling indeed plays an important role in enhancing performance. Aside from that, the LiRAP-coated NCM85 cathodes were found to exhibit increased cycling stability over the uncoated counterpart. Among the surface-protected materials studied, LHC@NCM85 delivered the highest initial specific discharge capacity and Coulomb efficiency, emphasizing the beneficial effect of the antiperovskite "shell". Furthermore, long-term cycling tests revealed superior capacity retention for all coated samples, with notable improvements achieved with the LHCB@NCM85 and LHCB:LNbO(0.5)@NCM85 cathodes.

Taken together, the results collectively demonstrate the efficacy of the melt-infiltration method for "functionalizing" industrially relevant CAMs using low-melting-point LiRAPs. The protective coatings serve to stabilize the CAM|SE interface and suppress adverse degradation mechanisms, thereby enhancing the electrochemical performance and stability of thiophosphate-based SSBs.

## *Acknowledgements*

This work was supported by BASF SE.

Open Access funding enabled and organized by Projekt DEAL.

## *Conflict of Interest*

The authors declare no conflict of interest.

## *Author Contributions*

**Philip Henkel**: formal analysis (lead); investigation (lead); writing—original draft (lead). **Ruizhuo Zhang**: formal analysis (supporting); investigation (supporting); writing—review & editing: (supporting). **Rajib Sahu**: formal analysis (supporting); investigation (supporting); writing—review & editing (supporting). **Christian Kübel**: formal analysis (supporting); writing—review & editing (supporting). **Jürgen Janek**: funding acquisition (equal); project administration (equal); supervision (equal); writing—review & editing (supporting). **Aleksandr Kondrakov**: conceptualization (lead); funding acquisition (equal); project administration (equal); supervision (equal); writing—review & editing (supporting). **Torsten Brezesinski**: conceptualization (lead); funding acquisition (equal); project administration (equal); supervision (lead); writing—review & editing (lead).

## *Data Availability Statement*

The data that support the findings of this study are available from the corresponding author upon reasonable request.

**Keywords:** all-solid-state batteries · antiperovskites · cathode particle coating · interfacial degradation · melt-infiltration

[1] A. Banerjee, X. Wang, C. Fang, E. A. Wu, Y. S. Meng, *Chem. Rev.* **2020**, *120*, 6878.
[2] Y.-G. Lee, S. Fujiki, C. Jung, N. Suzuki, N. Yashiro, R. Omoda, D.-S. Ko, T. Shiratsuchi, T. Sugimoto, S. Ryu, J. H. Ku, T. Watanabe, Y. Park, Y. Aihara, D. Im, I. T. Han, *Nat. Energy* **2020**, *5*, 299.
[3] T. Inada, K. Takada, A. Kajiyama, M. Kouguchi, H. Sasaki, S. Kondo, M. Watanabe, M. Murayama, R, *Solid State Ionics* **2003**, *158*, 275.
[4] D. Lin, Y. Liu, Y. Cui, *Nat. Nanotechnol.* **2017**, *12*, 194.
[5] Z. Gao, H. Sun, L. Fu, F. Ye, Y. Zhang, W. Luo, Y. Huang, *Adv. Mater.* **2018**, *30*, 1705702.
[6] A. Varzi, R. Raccichini, S. Passerini, B. Scrosati, *J. Mater. Chem. A* **2016**, *4*, 17251.
[7] J. Schnell, T. Günther, T. Knoche, C. Vieider, L. Köhler, A. Just, M. Keller, S. Passerini, G. Reinhart, *J. Power Sources* **2018**, *382*, 160.
[8] B.-X. Shi, Y. Yusim, S. Sen, T. Demuth, R. Ruess, K. Volz, A. Henss, F. H. Richter, *Adv. Energy Mater.* **2023**, *12*, 2300310.
[9] P. Minnmann, F. Strauss, A. Bielefeld, R. Ruess, P. Adelhelm, S. Burkhardt, S. L. Dreyer, E. Trevisanello, H. Ehrenberg, T. Brezesinski, F. H. Richter, J. Janek, *Adv. Energy Mater.* **2022**, *12*, 2201425.
[10] R. Ruess, S. Schweidler, H. Hemmelmann, G. Conforto, A. Bielefeld, D. A. Weber, J. Sann, M. T. Elm, J. Janek, *J. Electrochem. Soc.* **2020**, *167*, 100532.
[11] R. Koerver, W. Zhang, L. de Biasi, S. Schweidler, A. O. Kondrakov, S. Kolling, T. Brezesinski, P. Hartmann, W. G. Zeier, J. Janek, *Energy Environ. Sci.* **2018**, *11*, 2142.
[12] F. Han, Y. Zhu, X. He, Y. Mo, C. Wang, *Adv. Energy Mater.* **2016**, *6*, 1501590.
[13] Y. Zhu, X. He, Y. Mo, *ACS Appl. Mater. Interfaces* **2015**, *7*, 23685.
[14] R. Koerver, F. Walther, I. Aygün, J. Sann, C. Dietrich, W. G. Zeier, J. Janek, *J. Mater. Chem. A* **2017**, *5*, 22750.
[15] S. P. Culver, R. Koerver, W. G. Zeier, J. Janek, *Adv. Energy Mater.* **2019**, *9*, 1900626.
[16] D. Weber, Đ. Tripković, K. Kretschmer, M. Bianchini, T. Brezesinski, *Eur. J. Inorg. Chem.* **2020**, *2020*, 3117.
[17] Y. Ma, R. Zhang, Y. Tang, Y. Ma, J. H. Teo, T. Diemant, D. Goonetilleke, J. Janek, M. Bianchini, A. Kondrakov, T. Brezesinski, *ACS Nano* **2022**, *16*, 18682.
[18] Y. Ma, R. Zhang, Y. Ma, T. Diemant, Y. Tang, S. Payandeh, D. Goonetilleke, D. Kitsche, X. Liu, J. Ling, A. Kondrakov, T. Brezesinski, *Chem. Mater.* **2024**, *36*, 2588.
[19] Z. Chen, D. Chao, J. Lin, Z. Shen, *Mater. Res. Bull.* **2017**, *96*, 491.
[20] S. Payandeh, F. Strauss, A. Mazilkin, A. Kondrakov, T. Brezesinski, *Nano Res. Energy* **2022**, *1*, 9120016.
[21] A.-Y. Kim, F. Strauss, T. Bartsch, J. H. Teo, T. Hatsukade, A. Mazilkin, J. Janek, P. Hartmann, T. Brezesinski, *Chem. Mater.* **2019**, *31*, 9664.

[22] Z. Deng, D. Ni, D. Chen, Y. Bian, S. Li, Z. Wang, Y. Zhao, *InfoMat* **2022**, *4*, e12252.
[23] J. Zheng, B. Perry, Y. Wu, *ACS Mater. Au* **2021**, *1*, 92.
[24] W. Feng, L. Zhu, X. Dong, Y. Wang, Y. Xia, F. Wang, *Adv. Mater.* **2023**, *35*, 2210365.
[25] A.-Y. Song, Y. Xiao, K. Turcheniuk, P. Upadhya, A. Ramanujapuram, J. Benson, A. Magasinski, M. Olguin, L. Meda, O. Borodin, G. Yushin, *Adv. Energy Mater.* **2018**, *8*, 1700971.
[26] Y. Xiao, K. Turcheniuk, A. Narla, A.-Y. Song, X. Ren, A. Magasinski, A. Jain, S. Huang, H. Lee, G. Yushin, *Nat. Mater.* **2021**, *20*, 984.
[27] Y. Li, W. Zhou, S. Xin, S. Li, J. Zhu, X. Lü, Z. Cui, Q. Jia, J. Zhou, Y. Zhao, J. B. Goodenough, *Angew. Chem., Int. Ed.* **2016**, *55*, 9965.
[28] J. A. Dawson, T. S. Attari, H. Chen, S. P. Emge, K. E. Johnston, M. S. Islam, *Energy Environ. Sci.* **2018**, *11*, 2993.
[29] Y. Zhao, L. L. Daemen, *J. Am. Chem. Soc.* **2012**, *134*, 15042.
[30] H. J. Lee, B. Darminto, S. Narayanan, M. Diaz-Lopez, A. W. Xiao, Y. Chart, J. H. Lee, J. A. Dawson, M. Pasta, *J. Mater. Chem. A* **2022**, *10*, 11574.
[31] W. Xia, Y. Zhao, F. Zhao, K. Adair, R. Zhao, S. Li, R. Zou, Y. Zhao, X. Sun, *Chem. Rev.* **2022**, *122*, 3763.
[32] Z. D. Hood, H. Wang, A. S. Pandian, J. K. Keum, C. Liang, *J. Am. Chem. Soc.* **2016**, *138*, 1768.
[33] Y. Zhang, Y. Zhao, C. Chen, *Phys. Rev. B* **2013**, *87*, 134303.
[34] G. Schwering, A. Hönnerscheid, L. van Wüllen, M. Jansen, *ChemPhysChem* **2003**, *4*, 343.
[35] J. Howard, Z. D. Hood, N. A. W. Holzwarth, *Phys. Rev. Mater.* **2017**, *1*, 075406.
[36] J. Zheng, J. Elgin, J. Shao, Y. Wu, *eScience* **2022**, *2*, 639.
[37] K. Yoshikawa, T. Yamamoto, M. K. Sugumar, M. Motoyama, Y. Iriyama, *Energy Fuels* **2021**, *35*, 12581.
[38] D. H. S. Tan, E. A. Wu, H. Nguyen, Z. Chen, M. A. T. Marple, J.-M. Doux, X. Wang, H. Yang, A. Banerjee, Y. S. Meng, *ACS Energy Lett.* **2019**, *4*, 2418.

Manuscript received: July 15, 2025
Revised manuscript received: August 8, 2025
Version of record online: